

Pressure distribution imaging through wide-field optical detected magnetic resonance

Chaofan Lv(吕超凡), Kai Ma(马凯), Feihu Lei(雷飞虎), Yidan Qu(屈怡丹), Qilong Wu(吴琦隆), Wuyou Zhang(张吾优), Yingjie Zhang(张英杰), Huihui Yu(余辉辉), Xuanming Shen(申炫铭), Yuan Zhang(张元), Xigui Yang(杨西贵), and Chongxin Shan(单崇新)

Citation: Chin. Phys. B, 2025, 34 (**8**): 087601. DOI: 10.1088/1674-1056/addbc9
http://cpb.iphy.ac.cn; http://iopscience.iop.org/cpb

What follows is a list of articles you may be interested in

Gas encapsulation technology for large volume press

Minghao Du(杜明浩) and Duanwei He(贺端威)
Chin. Phys. B, 2024, 33 (**11**): 110701. DOI: 10.1088/1674-1056/ad7af8

Anti-Stokes/Stokes temperature calibration and its application in laser-heating diamond anvil cells

Minmin Zhao(赵旻旻), Binbin Wu(吴彬彬), Jingyi Liu(刘静仪), and Li Lei(雷力)
Chin. Phys. B, 2023, 32 (**9**): 090704. DOI: 10.1088/1674-1056/accd55

Experimental investigation of vector static magnetic field detection using an NV center with a single first-shell ^{13}C nuclear spin in diamond

Feng-Jian Jiang(蒋峰建), Jian-Feng Ye(叶剑锋), Zheng Jiao(焦铮), Jun Jiang(蒋军), Kun Ma(马堃), Xin-Hu Yan(闫新虎), Hai-Jiang Lv(吕海江)
Chin. Phys. B, 2018, 27 (**5**): 057602. DOI: 10.1088/1674-1056/27/5/057602

Estimation of vector static magnetic field by a nitrogen-vacancy center with a single first-shell ^{13}C nuclear (NV-^{13}C) spin in diamond

Feng-Jian Jiang(蒋峰建), Jian-Feng Ye(叶剑锋), Zheng Jiao(焦铮), Zhi-Yong Huang(黄志永), Hai-Jiang Lv(吕海江)
Chin. Phys. B, 2018, 27 (**5**): 057601. DOI: 10.1088/1674-1056/27/5/057601

High contrast atomic magnetometer based on coherent population trapping

Yang Ai-Lin (杨爱林), Yang Guo-Qing (杨国卿), Xu Yun-Fei (徐云飞), Lin Qiang (林强)
Chin. Phys. B, 2014, 23 (**2**): 027601. DOI: 10.1088/1674-1056/23/2/027601

SPECIAL TOPIC — Structures and properties of materials under high pressure

Pressure distribution imaging through wide-field optical detected magnetic resonance

Chaofan Lv(吕超凡)[1,2,3,†], Kai Ma(马凯)[1,†], Feihu Lei(雷飞虎)[1], Yidan Qu(屈怡丹)[1], Qilong Wu(吴琦隆)[1], Wuyou Zhang(张吾优)[1], Yingjie Zhang(张英杰)[1], Huihui Yu(余辉辉)[1], Xuanming Shen(申炫铭)[1], Yuan Zhang(张元)[1,‡], Xigui Yang(杨西贵)[1,§], and Chongxin Shan(单崇新)[1,¶]

[1] *Henan Key Laboratory of Diamond Optoelectronic Materials and Devices, Key Laboratory of Integrated Circuit, Ministry of Education, School of Physics, Zhengzhou University, Zhengzhou* 450001, *China*

[2] *State Key Laboratory of Luminescence and Applications, Changchun Institute of Optics, Fine Mechanics and Physics, Chinese Academy of Sciences, Changchun* 130033, *China*

[3] *Center of Materials Science and Optoelectronics Engineering, University of Chinese Academy of Sciences, Beijing* 100049, *China*

(Received 25 February 2025; revised manuscript received 8 May 2025; accepted manuscript online 22 May 2025)

Non-hydrostatic stress plays a significant role in shaping the properties of materials under compression. High-pressure effects such as yielding deformation, phase transitions, and volume contraction can alter the pressure distribution within the pressure chamber. However, due to the inherent size limitation of the diamond anvil cell (DAC), *in situ* high-pressure studies usually assume a hydrostatic environment, equaling the pressure of samples to a pressure calibrator inside the chamber. Accurately imaging pressure distribution within the DAC chamber remains challenging, particularly as the material undergoes phase transitions. Here, we present a method for mapping pressure distribution with high spatial resolution using wide-field optically detected magnetic resonance (ODMR) of nanodiamonds. The pressure gradients during the high-pressure transition of zinc oxide (ZnO) were compared using both the multiple rubies technique and wide-field ODMR. The latter technique demonstrated superior spatial resolution, easier operation, and more detailed information. These results highlight the potential of wide-field ODMR as a powerful tool for precise pressure sensing, particularly in studies involving non-hydrostatic pressure conditions.

Keywords: optically detected magnetic resonance (ODMR), high-pressure, phase transition, ZnO

PACS: 76.70.Hb, 07.35.+k, 64.70.Nd, 81.05.ug, 61.50.Ks

DOI: 10.1088/1674-1056/addbc9 **CSTR:** 32038.14.CPB.addbc9

1. Introduction

Pressure, as an independent thermodynamic parameter, has proven to be an effective and clean stimulus for tuning the structural and electronic configurations of materials. High-pressure techniques have revealed many unusual and important phenomena, including pressure-induced phase transitions, novel emission states, superconductivity and the synthesis of metastable materials.[1–3] Benefiting from the good applicability of various optical and electronic characterization systems, the diamond anvil cell (DAC) has been the most widely used equipment for pressure generation and *in situ* measurement. However, uniaxial compression in DAC introduces considerable radial pressure gradient without pressure transmitting medium (PTM),[4–6] or other non-hydrostatic pressure conditions due to the solidification of PTM and the squeezing of polycrystal grains.[7,8] Nevertheless, it is reported that non-hydrostatic pressure drastically changes the mechanism and kinetics of phase transitions,[9–15] facilitating the transition of sp^2 union carbon to sp^3 diamond,[12] reducing the conversion potential barrier between h-BN and w-BN,[16] triggering the aggregation of semiconductor quantum dots and the formation of nano chains, superlattices or other nanostructures,[17–19] or even inducing superconductivity and a transition from fragility to elasticity of diamond.[2,9,20,21] Phase transition, morphology alteration and the accompanied redistribution of pressure, or even further pressure loading would change the pressure distribution in the DAC chamber.[22] Thus, precise pressure calibration still plays a critical role in ensuring the accuracy of *in situ* research under non-hydrostatic pressure.

Current *in situ* pressure calibration methods face limitations due to the bulky nature of existing calibrators. Fluorescent ruby and equations of state (EOS) methods, for example, are restricted by their spatial resolution and inadequate for non-hydrostatic pressure research.[23] The negatively charged nitrogen-vacancy (NV) center, i.e., a point defect in the diamond lattice, consists of a substitutional nitrogen atom, an

[†]These authors contributed equally to this work.
[‡]Corresponding author. E-mail: yzhuaudipc@zzu.edu.cn
[§]Corresponding author. E-mail: yangxg@zzu.edu.cn
[¶]Corresponding author. E-mail: cxshan@zzu.edu.cn

© 2025 Chinese Physical Society and IOP Publishing Ltd. All rights, including for text and data mining, AI training, and similar technologies, are reserved.

adjacent carbon vacancy, and a captured electron.[24] The NV center has a triplet ground and excited state, as well as two singlet metastable states, and the spin levels of the ground state are separated in frequency by a so-called zero-field-splitting D_{gs}. Upon excitation by a laser with e.g., 532 nm wavelength, the NV centers can decay via spin-preserved radiative channels, or spin-inverted non-radiative channels, which enables spin initialization and readout by optical means. Combining further with microwave absorption of the NV spin, the electron spin resonance spectrum can be measured with the so-called optically detected magnetic resonance (ODMR) technique. It was observed that the experimentally extracted D_{gs} from the ODMR spectrum was sensitive to local environment, such as magnetic field, electric field, strain, and temperature. The superb spatial resolution and robust optical interface sustain extreme pressure, providing a simple and efficient method for sensing local perturbations under high pressure. D_{gs} was shown to increase linearly with pressure with a slope of 14.6 MHz/GPa up to 130 GPa,[25,26] and was used to reconstruct the stress-tensor with high spatial resolution.[27] Shallow implanted NV centers on the surface of the diamond anvil were also used to probe the magnetization of Fe particles and the Meissner effect of a superconductor, and to construct the full stress tensor on the culet surface,[28–30] but this stress in the anvil exhibited aberration with the pressure inside the chamber. Multiple micrometer-sized diamond particles with NV centers have been placed inside the DAC chamber to compare various pressures point by point during the solidification of Daphne oil 7373 under compression.[31] However, the scanning process requires considerable time, which significantly limits its practical application in time-sensitive experiments. It is therefore important to explore fast methods for pressure imaging inside the pressure chamber and compare the pressure distribution during the phase transition processes of the sample.

In this work, a feasible pressure imaging method was realized through wide-field ODMR spectra of spread NV nanodiamonds inside the DAC chamber. To ensure effective sensing under high pressure, the NV nanodiamonds were characterized in detail. A wide-field ODMR setup was built to enable the *in situ* pressure imaging under compression. The pressure distribution evolution during the high-pressure phase transition of ZnO was systematically monitored with NV nanodiamonds and multiple rubies, respectively, and a distinct pressure gradient reversal following the phase transition was revealed. Compared with conventional multiple-ruby technique, the wide-field ODMR pressure imaging method demonstrates superior performance in terms of operational feasibility, spatial resolution, and measurement accuracy. This innovative approach provides a reliable solution for precise visualization of pressure distribution and its dynamic evolution within the DAC chamber, offering promising potential for advancing non-hydrostatic pressure-related research.

2. Methods

2.1. Materials

Nanodiamonds with an NV center density of ~ 2 ppm were purchased from Adamas Nanotechnologies. The ZnO nanocrystals were synthesized via a hydrothermal process. A 0.9 M zinc acetate solution was prepared by dissolving 2.00 g of $Zn(OAc)_2{\cdot}2H_2O$ in 10 ml of ethanol and stirring for 30 min at room temperature. After the stirring period, a suspension was obtained after stirring. Then, the solution was transferred to a stainless-steel autoclave in a 25 ml Teflon vessel and heated at 200 °C for several minutes. The sample was then automatically cooled down to room temperature. Afterward, the precipitate was collected by centrifugation at 7000 rpm for 5 min and washed with ethanol three times to wash off impurities. Before each centrifugation, the as-prepared sample was sonicated for 15 minutes. Subsequently, the white precipitate was dried in a blast oven at 60 °C overnight.

2.2. Characterizations

The scanning electron microscope (SEM) image of the samples was acquired by JEOL JSM-6700F field-emission scanning electron microscope. The x-ray diffraction (XRD) was recorded with Cu $K\alpha$ radiation (D8 Discover, Bruker, Germany). The *in situ* high-pressure Raman spectra were detected using a home-built Raman spectrometer. A single-mode diode pumped solid state (DPSS) laser with a wavelength of 532 nm (CNI MSL-III-532 100 mW) was employed for excitation. A razor-edge Raman filter (Semrock LP02-532RE-25) was used to reflect the laser light. A long working distance objective (Olympus SLMPLN 20X) was used for the excitation and collection of the scattered light, the residual laser light was filtered with another razor-edge Raman filter (Semrock LP02-532RE-25). The Raman light was then imaged onto a charge-coupled device (CCD) camera (Princeton Instruments PIXIS 256) embedded in a monochromator (Princeton Instruments SP 2500i), a grating of 1200 groove/mm offering a resolution of 1 cm^{-1}.

The photoluminescence (PL) experiments with 355 nm excitation were performed using a home-built PL microscope (BX-53 Olympus). A single-mode DPSS laser (CNI UV-F-355 10 mW) provided excitation. Fluorescence was collected through a 10× UV Plan apochromatic objective, spectrally separated by a dichroic mirror (Semrock Di01-R355-25x36), and filtered with a 355 nm long-pass filter (Semrock BLP01-355R-25). The PL was imaged onto a CCD camera (Princeton Instruments PIXIS 256) within a monochromator (Princeton Instruments SP 2500i) equipped with a 300 groove/mm grating.

PL experiments with 532 nm excitation were similarly conducted using the same microscope. Excitation was provided by a DPSS laser (CNI MSL-III-532 100 mW). Fluorescence collection and filtering were analogous to the 355 nm setup, using a 10× UV Plan apochromatic objective, dichroic mirror (Semrock Di01-R532-25x36), and a 532 nm long-pass filter (Semrock BLP01-532R-25). The signal was detected by the same CCD camera and monochromator system with a 300 groove/mm grating.

PL decay measurements used the BX-53 microscope with excitation from a 378 nm picosecond pulsed diode laser (NKT Photonics PIL037-FS). Fluorescence was collected through a 10× UV plan apochromatic objective and directed into a grating spectrometer (SP-2400i SOL) coupled to a PMT (Hamamatsu PMH-100) connected to a photon-counting card (BH SP-150). A 1 nm spectral resolution was achieved with a 200 μm slit.

2.3. High-pressure generation

The DAC was made of nonmagnetic beryllium copper alloy. Pressure was generated from a pair of anvils of IIa type diamond, with 500 μm culets, and high-pressure conditions were provided by the DAC. The sample chamber was a 150-μm-diameter hole drilled at the center of the pre-indented T301 gasket with a thickness of approximately 60 μm. The standard ruby fluorescence technique was applied to calibrate the pressure during compression.

2.4. High-pressure ODMR

The wide-field ODMR under pressure was conducted with a home-built ODMR system. A single-mode DPSS laser with a wavelength of 532 nm (CNI MSL-III-532 100 mW) was employed for excitation. A plano-convex lens with 100 mm focal length before the objective was used to acquire wide-field laser illumination, a long working distance objective (Olympus SLMPLN 20X) was used for the excitation and collection of the PL light of NV nanodiamonds, a black-and-white digital camera (MER3-506-58G3M-P) embedded in a microscope (BX-53 Olympus) was used to collect the PL light and track the PL contrast. A long working distance objective is used to focus the green laser beam onto the DAC culet, and to collect the NV center fluorescence signals. A single-chip microcomputer (STM32) was used to generate a microwave sweep, and a power amplifier amplified the microwave to 20 dBm.

To carry out the ODMR measurement under high pressure, a beryllium-copper DAC with a pair of low-fluorescence diamond anvils and an integrated platinum microwave antenna was used and placed at the corner of the DAC chamber, which was further connected to the external microwave cable. The high-pressure sample chamber was enclosed by two diamond anvils and a beryllium-copper gasket. We used c-BN powder mixed with epoxy to insulate the platinum wire from the beryllium-copper gasket. The T1, T2, and Rabi oscillation of NV nanodiamonds were measured with a diamond single quantum spin spectrometer (CIQTEK Diamond II).

All the experiments were carried out at ambient temperature.

3. Results

To establish the suitability of NV nanodiamonds as reliable pressure sensors under extremely high-pressure conditions, a comprehensive characterization of their fundamental physical and optical properties was conducted first.[32] Figure 1(a) presents a scanning electron microscopy (SEM) image illustrating the morphological characteristics of the nanodiamonds. The micrograph reveals particles with well-defined shapes, flat surfaces, and uniform grain sizes. According to statistical analysis of the grain size distribution (Fig. 1(b)), the NV diamonds exhibit grain size from 500 nm to 1.2 μm, with an average grain diameter of 723 nm. The sub-micron dimensions, approaching the optical diffraction limit, enable exceptional spatial resolution in pressure sensing. The XRD pattern in Fig. 1(c) exhibits distinct (111), (220), and (311) diffraction peaks,

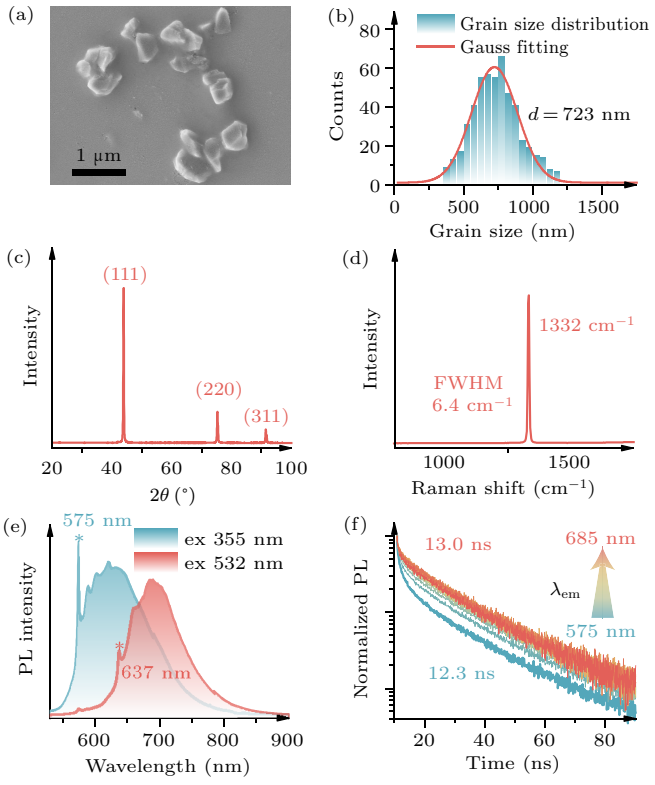


Fig. 1. Characterization of the NV nanodiamonds. Typical SEM image (a) and the corresponding grain size distribution (b) of the NV nanodiamonds. XRD pattern (c) and Raman spectrum (d) of the NV nanodiamonds. (e) Photoluminescence (PL) spectrum of the NV nanodiamonds under 355 nm and 532 nm laser excitation. (f) PL decay of the NV nanodiamonds, monitored at 575 nm and 637 nm, respectively.

confirming the high crystallinity.[33] Furthermore, Raman spectroscopic analysis reveals a pure sp^3 hybridized phase, as evidenced by a sharp peak with a full width at half maximum of 6.4 cm^{-1} and the absence of any sp^2 characteristic signals.[34] These structural characteristics guarantee exceptional stability of the NV nanodiamonds under pressure, in both physical and chemical properties. Under dual-wavelength laser excitation at 355 nm and 532 nm, the NV nanodiamonds demonstrate distinct PL spectral characteristics, which are attributed to the selective excitation of the neutral and negatively charged NV centers. Notably, only the latter exhibits radiative emission over 600 nm exclusively under green light (532 nm) excitation. Furthermore, time-resolved PL measurements reveal a wavelength-dependent lifetime prolongation, with the PL lifetime increasing from 12.3 ns at 575 nm to 13.0 ns at 685 nm.

As illustrated in Fig. 2(a), the NV center consists of a substitutional nitrogen atom adjacent to a carbon vacancy in the diamond lattice. When an additional electron is captured, the neutral NV center transforms into the negatively charged NV center, which has a triplet ground and excited state, and two singlet metastable states (not shown).[35] Upon excitation by a laser with, e.g., 532 nm wavelength, the NV centers can decay via spin-preserved radiative channels, or spin-inverted non-radiative channels, which enables high-fidelity optical spin-state initialization and readout.[36] Upon microwave excitation, the $|0\rangle$ state can be resonantly excited to the $|\pm 1\rangle$ states, and the fluorescence from the NV centers becomes reduced. By varying the microwave frequency, one can obtain the so-called ODMR spectra, as shown in Fig. 2(b). From these spectra, one can extract a zero-field splitting around $D_{gs} = 2.87$ GHz, consistent with previous reports.[37] Extensive research has demonstrated that the zero-field splitting parameter D_{gs} exhibits remarkable sensitivity to local environmental perturbations, establishing NV centers as versatile quantum sensors of magnetic fields, temperatures, pressures, and electric fields.[28–30,38,39]

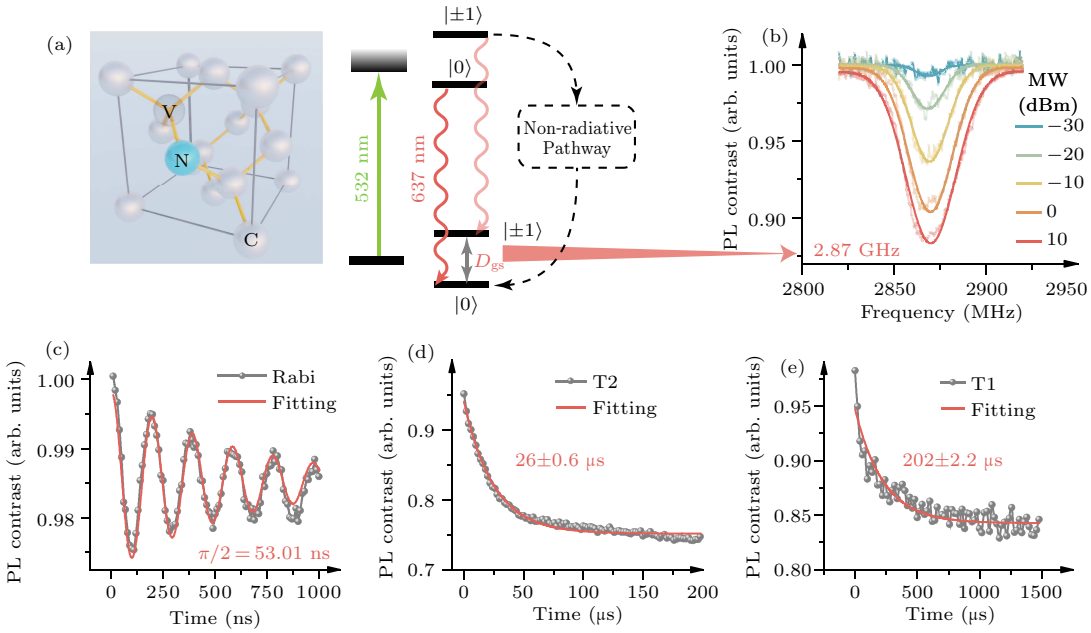


Fig. 2. Schematic illustration of the optically detected magnetic resonance (ODMR) in the NV center and the coherent quantum control of NV centers. (a) Structure and energy-level scheme of the NV center in diamond. (b) ODMR spectra of the NV nanodiamonds under microwave excitation at different power levels. (c) Rabi oscillations of the NV nanodiamonds under ambient pressure. Typical (d) spin relaxation signal, and (e) spin echo signal under ambient pressure.

To establish the robustness of quantum spin properties for sensing applications under extreme conditions, we systematically characterized the spin dynamics of nanodiamonds inside the diamond anvil at ambient pressure. To this end, we first align the external magnetic field of 50 Gauss along one NV axis, and confirm the alignment through the ODMR spectrum. Then, we tune the microwave field to be resonant with the $|0\rangle \rightarrow |+1\rangle$, and apply the laser, microwave, and readout pulse to carry out the Rabi oscillation experiment, a microwave power of 10 dBm and a laser intensity of 3 mW are applied, respectively. Here, the fluorescence is detected by a single-photon detector after properly attenuating the strong fluorescence with a neutral density filter. The Rabi oscillation shown in Fig. 2(c) demonstrates the coherent control of spins with a $\pi/2$ time of 53.01 ns. With this time, we carry out the Hahn echo experiment with the pulse sequences, and obtain the results shown in Fig. 2(d). By fitting the curve with an exponential function, we obtain a long coherence time of 26 ± 0.6 μs. In addition, we also carry out the relaxometry experiment and obtain a spin-lattice relaxation time of

202 ± 2.2 μs (Fig. 2(e)). This observation aligns with the previously characterized crystallinity and clean surface morphology, suggesting promising potential for sensing applications under high pressure.

Subsequently, we performed continuous wave ODMR measurements under compression. Figures 3(a) and 3(b) display the PL contrast as a function of microwave frequency, along with the extracted pressure-dependent resonance peak positions. The ODMR spectra exhibit slight splitting due to the variation of the local strain, and this is most pronounced with low microwave and laser power. Following commonly used methods reported previously,[25] the resonance peaks are analyzed using a dual-Lorentzian fitting model to extract the midpoint frequency between the two sub-peaks as the D_{gs}, which reveals a linear dependence on pressure

$$\frac{dD_{gs}}{dP} = 14.14 \pm 0.34\ (\mathrm{MHz \cdot GPa^{-1}}). \tag{1}$$

This increment under pressure originates from the shrinking of the distance between the atoms due to both the macroscopic compression of the diamond lattice and local structural distortions at the NV defect site.[40] The slope is marginally smaller than previously reported results, which is likely due to the absence of a PTM in the present study.[26,31,41,42] The sensitivity of the nanodiamond-based pressure sensor was further evaluated. As shown in Fig. 3(c), a noise-limited sensitivity of 0.045 GPa·Hz$^{1/2}$ is extracted from a time series consisting of 50 consecutive measurements under 1.0 GPa pressure, demonstrating excellent sensor performance.

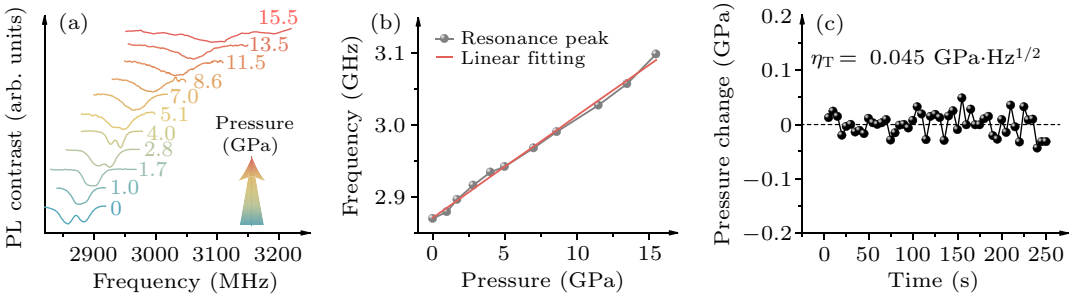


Fig. 3. ODMR spectra under high pressure. (a) ODMR spectra of NV centers in nanodiamonds under various pressures. (b) The NV zero-field splitting D_{gs} as a function of pressure. (c) Time series of pressure sensing demonstrates a noise floor of 0.045 GPa·Hz$^{1/2}$, monitored at 1.0 GPa.

The pressure distribution and its evolution under non-hydrostatic conditions remain poorly understood, particularly during high-pressure phase transition processes. To investigate variations in pressure distribution during a phase transition, ZnO, undergoing a hexagonal-to-cubic transition under pressure, was selected. The volume contraction of the unit cell during this phase transition leads to changes in the pressure distribution within the DAC chamber. Given the morphological diversity of ZnO, it provides an adjustable stress environment under compression. Numerous studies have reported intriguing stress-dependent optoelectrical properties of ZnO, including piezoelectric-assisted low-threshold lasing and novel stress-induced self-trapped exciton emission.[43] In this study, we focus on ZnO to investigate its pressure distribution and evolution under varying pressure conditions, and no PTM was used.

The high-pressure phase transition was confirmed through *in situ* Raman spectroscopy. As shown in Fig. 4(a), ZnO exhibits Raman eigenmodes E_2 (low), E_2 (high), and A_1 (TO) at 101 cm^{-1}, 437 cm^{-1}, and 576 cm^{-1}, respectively. Under compression, all Raman peaks shift linearly up to 7.0 GPa, where their weakening and disappearance mark the onset of the wurtzite to rocksalt structural (B1 phase) transition, in excellent agreement with the previous report.[44] Upon further compression, new broad bands emerge at 150 cm^{-1} and 562 cm^{-1}, indicating the completation of the phase transition to the B1 phase.[45,46]

To assess the pressure distribution within the DAC chamber, we applied the traditional multiple-ruby PL-mapping method, and loaded a total of 18 rubies inside the DAC chamber. The rubies are indicated by gray circles in the optical image (Fig. 4(c)) and appear as black dots in the PL mapping image (Fig. 4(d)). The emission spectra of these rubies were collected to extract pressure information, summarized in extended Fig. S1 and Table S1. The pressure in the chamber is represented as the average pressure of 18 rubies (P_{avr}). Using the ruby with the lowest pressure as a reference, the pressure differences (ΔP) of the other rubies under compression are illustrated in the calculated images (Figs. 4(e)–4(k)). A slight ΔP difference is observed at 1.0 GPa (Fig. 4(e)), which increases at 4.2 GPa, revealing a positive pressure gradient (P_{Gra}) from the chamber's center toward the edge, as indicated by the colored arrows (Figs. 4(f) and 4(g)). With further compression to 7.8 GPa, the P_{Gra} decreases, evidenced by an increased ΔP at the chamber center, likely due to changes in the unit cell volume of ZnO and stress redistribution during the phase transition.[22] The reversal of the P_{Gra} is completed at 8.5 GPa, leading to a further increase in the negative P_{Gra} as pressure rises to 14.0 GPa. The average pressure at varying radii as a function of the radius is depicted in Fig. 4(l) and summarized

in Fig. 4(m). Initially, the pressure distribution is nearly uniform, with a zero P_{Gra}. As compression progresses, a positive P_{Gra} develops until the phase transition triggers stress redistribution, which reduces the positive P_{Gra}. Notably, the completed phase transition reverses the P_{Gra} orientation, ultimately resulting in a negative P_{Gra} reaching −38 GPa/mm. However, the ruby PL-mapping method, employing a scan step of 3 μm and an exposure time of 0.5 s per point, requires approximately 2 hours for imaging, and shows inherent limitations in both spatial resolution and acquisition speed.

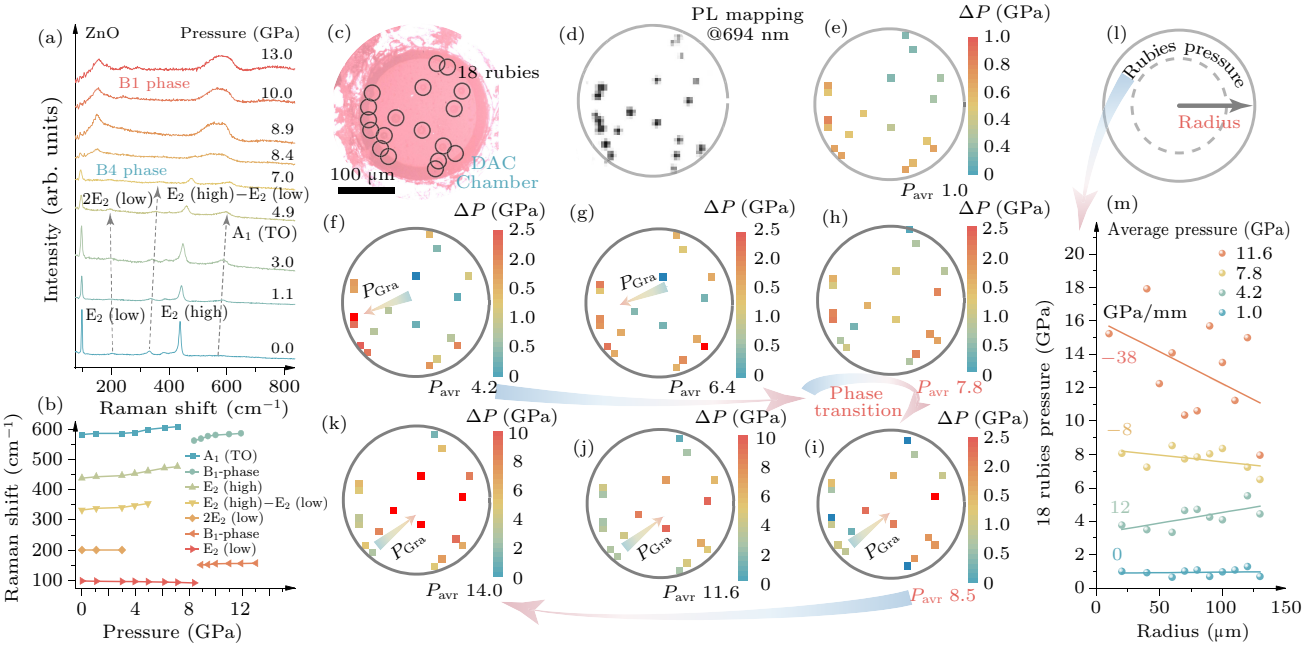


Fig. 4. Pressure distribution monitored with the ruby PL-mapping method. (a) Raman spectra of ZnO under selected pressures. (b) Raman peak positions as functions of pressure. (c) A microscopic image of the DAC pressure chamber containing ZnO powder and 18 rubies, marked with gray circles. (d) PL-mapping image of 18 rubies inside the DAC pressure chamber, monitored at 694 nm. (e)–(k) Images of the pressure difference (ΔP) of 18 rubies inside the DAC chamber. Gradual color arrows from green to red indicate the pressure gradient. All the scale bars of (d)–(e) are the same as (c), and are omitted for a brevity. (l) Schematic illustration of the average pressure at varying radii and (m) corresponding average pressure as functions of the radius under selected pressures, as well as the linear fitting lines. Gradual colored arrows from blue to red serve only as indicators.

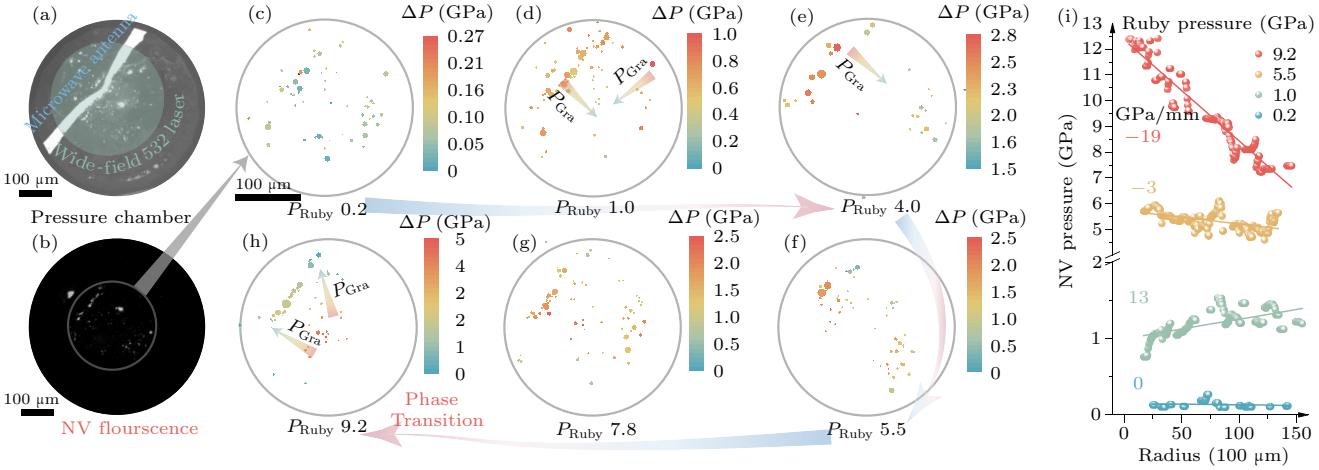


Fig. 5. Pressure distribution imaging conducted with the wide-field ODMR technique. (a) Bright field microscopic image of the DAC chamber. Metal wire: gold microwave antenna. Circular green area: pressure chamber illuminated with wide-field 532 nm laser. (b) Dark field PL image of the nanodiamonds in the DAC chamber, and the red circle indicating the region of interest considered in the wide-field ODMR experiments. (c)–(h) Spatial distribution of pressure difference (ΔP) of the NV nanodiamonds under various pressures. P_{Ruby}, Pressure estimated from the ruby at the reverse side of the chamber. Gradual color arrows from green to red indicate P_{Gra}. All the scale bars of (d)–(h) are the same as (c) and are omitted for brevity. (i) Average pressure as a function of the radius under selected pressures, and corresponding linear fitting lines, extracted from the pressure distribution imaging monitored with nanodiamonds.

As pressure calibrators, the nanodiamonds provide significantly higher spatial resolution than rubies. Particularly under wide-field laser illumination, the operation of nanodiamonds can be facilitated without the need for successive positioning and readout of the PL spectrum from rubies, enabling a fast and directed imaging scheme for pressure sensing. The exper-

iments are performed as shown by the micrographs taken from a monochrome camera shown in Fig. 5(a), nanodiamond clusters (bright white spots) inside the DAC chamber are illuminated with a wide-field 532 nm laser (translucent green area), and a platinum filament acts as the microwave antenna. The resulting fluorescence image (Fig. 5(b)) and intensity contrast of nanodiamonds under microwave sweep are captured and the resonance absorption peaks are extracted, allowing the calculation of pressure values for each nanodiamond from Eq. (1). A ruby located at the reverse side of the DAC chamber serves as a pressure reference.

In wide-field ODMR experiments, the spatial resolution is limited by the largest of the nanodiamond size (average 723 nm), the imaging objective's optical resolution (1.7 μm per the Rayleigh criterion), and the camera pixel size (2.74 μm, with a theoretical Nyquist limit of 73 nm). Consequently, the system's resolution is ultimately constrained to 1.7 μm, while the camera's direct imaging of pressure distribution reduces the total imaging time to 15 minutes, offering a remarkable improvements over ruby-based methods.

In Figs. 5(c)–5(h), due to slight deformation of the gasket under pressure, the ZnO nanocrystal powder exhibits mobility, while the nanodiamonds may be partially embedded or reappear upon compression. Thus, the automatically selected nanodiamonds show randomness to a certain extent. Nevertheless, the nanodiamonds previously uniformly dispersed consistently reflect the pressure distributions under compression. When the pressure is initially loaded to 0.2 GPa, its distribution inside the chamber is nearly uniform, with a ΔP less than 0.27 GPa (Fig. 5(c)). A prominent P_{Gra} appears at 1.0 GPa, as seen in Fig. 5(d), and the nanodiamonds in the top-left corner of the chamber agglomerate near the antenna, displaying a ΔP near 1.0 GPa. A positive P_{Gra} is observed from the chamber center to the edge, indicated by the colored arrows, which is similar to the phenomenon noted with rubies but provides much higher spatial resolution and prompt data acquisition. It continues to increase until reaching 4.0 GPa (Fig. 5(e)), at which point ΔP extends to 2.8 GPa, and begins to decrease at 5.5 GPa (Fig. 5(f)), when ΔP slightly drops to 2.5 GPa, and subsequently reverts to a negative P_{Gra} at 9.2 GPa, coinciding with the completion of the high-pressure phase transition.

In Fig. 5(i), the average pressure at specific radii as a function of radius is presented under selected pressures, derived from the nanodiamonds. This illustrates a similar trend of reversed P_{Gra} reaching -19 GPa/mm at 9.2 GPa. Notably, compared with the P_{Gra} obtained from rubies, the P_{Gra} obtained from the nanodiamonds provides more robust and detailed information due to their higher spatial resolution and increased number of sensing units.

4. Conclusion

In summary, we identified NV nanodiamonds as an ideal candidate for quantum pressure sensing inside the DAC chamber. Through comprehensive characterization, we confirmed their effectiveness under extreme conditions. By employing wide-field laser illumination and PL contrast tracking of dispersed NV nanodiamonds during a microwave sweep, we successfully achieved *in situ* pressure distribution imaging using wide-field ODMR. This technique enabled us to observe the pressure distribution and its evolution during the high-pressure phase transition of ZnO, revealing a unique orientation-reversed pressure gradient inside the chamber. This *in situ* imaging approach offers excellent performance, with high spatial resolution, sensitivity, and practical ease of use.

Acknowledgements

This work was supported by the National Key R&D Program of China (Grant No. 2024YFE0105200) and the National Natural Science Foundation of China (Grant Nos. 62422408, 12374016, 12174348, 62271450, 62027816, 12422413, and 62475242).

References

[1] Du M and He D 2024 *Chin. Phys. B* **33** 110701
[2] Liu C, Song X, Li Q, Ma Y and Chen C 2019 *Phys. Rev. Lett.* **123** 195504
[3] Lv R, Tu W, Shao D, Sun Y and Lu W 2023 *Chin. Phys. Lett.* **40** 117401
[4] Sung C, Goetze C and Mao H 1977 *Rev. Sci. Instrum.* **48** 1386
[5] Piermarini G J, Block S and Barnett J D 1973 *J. Appl. Phys.* **44** 5377
[6] Levitas V I, Dhar A and Pandey K K 2023 *Nat. Commun.* **14** 5955
[7] Bassett W A 2006 *J. Phys.: Condens. Matter* **18** S921
[8] Jiang S, Chen X, Huang X, Li C, Wang Z, Zhao B, Zhang L, Zhou G and Fang J 2024 *J. Am. Chem. Soc.* **146** 8598
[9] Song X, Liu C, Li Q, Hemley R J, Ma Y and Chen C 2022 *Proc. Natl. Acad. Sci.* **119** e2122691119
[10] Wang S, Zhao X, Hu K, Feng B, Hou X, Zhang Y, Liu S, Shang Y, Liu Z, Yao M and Liu B 2024 *Chin. Phys. B* **33** 098104
[11] Delogu F 2008 *Phys. Rev. Lett.* **100** 255901
[12] Dong J, Yao Z, Yao M, Li R, Hu K, Zhu L, Wang Y, Sun H, Sundqvist B, Yang K and Liu B 2020 *Phys. Rev. Lett.* **124** 065701
[13] Levitas V I, Ma Y, Hashemi J, Holtz M and Guven N 2006 *J. Chem. Phys.* **125** 044507
[14] Levitas V I 2004 *Phys. Rev. B* **70** 184118
[15] Turneaure S J, Sharma S M, Volz T J, Winey J M and Gupta Y M 2017 *Sci. Adv.* **3** e3561
[16] Ji C, Levitas V I, Zhu H, Chaudhuri J, Marathe A and Ma Y 2012 *Proc. Natl. Acad. Sci.* **109** 19108
[17] Li W, Fan H and Li J 2014 *Nano Lett.* **14** 4951
[18] Xiao T, Nagaoka Y, Wang X, Jiang T, LaMontagne D, Zhang Q, Cao C, Diao X, Qiu J, Lu Y, Wang Z and Cao Y C 2022 *Science* **377** 870
[19] Li B, Bian K, Zhou X, Lu P, Liu S, Brener I, Sinclair M, Luk T, Schunk H, Alarid L, Clem P G, Wang Z and Fan H 2017 *Sci. Adv.* **3** e1602916
[20] Zhu Y, Peng D, Zhang E, *et al.* 2024 *Nature* **631** 531
[21] Umeo K, Takikawa R, Onimaru T, Adachi M, Matsumoto K T and Takabatake T 2020 *Phys. Rev. B* **102** 094505
[22] Hemley R J, Mao H, Shen G, Badro J, Gillet P, Hanfland M and Häusermann D 1997 *Science* **276** 1242
[23] Mao H K, Xu J and Bell P M 1986 *J. Geophys. Res. Solid Earth* **91** 4673

[24] Siyushev P, Pinto H, Vörös M, Gali A, Jelezko F and Wrachtrup J 2013 *Phys. Rev. Lett.* **110** 167402

[25] Ho K O, Leung M Y, Reddy P, Xie J, Wong K C, Jiang Y, Zhang W, Yip K Y, Leung W K, Pang Y Y, Yu K Y, Goh S K, Doherty M W and Yang S 2022 *Phys. Rev. Appl.* **18** 064042

[26] Dai J H, Shang Y X, Yu Y H, Xu Y, Yu H, Hong F, Yu X H, Pan X Y and Liu G Q 2022 *Chin. Phys. Lett.* **39** 117601

[27] Broadway D A, Johnson B C, Barson M S J, Lillie S E, Dontschuk N, McCloskey D J, Tsai A, Teraji T, Simpson D A, Stacey A, McCallum J C, Bradby J E, Doherty M W, Hollenberg L C L and Tetienne J P 2019 *Nano Lett.* **19** 4543

[28] Hsieh S, Bhattacharyya P, Zu C, Mittiga T, Smart T J, Machado F, Kobrin B, Höhn T O, Rui N Z, Kamrani M, Chatterjee S, Choi S, Zaletel M, Struzhkin V V, Moore J E, Levitas V I, Jeanloz R and Yao N Y 2019 *Science* **366** 1349

[29] Lesik M, Plisson T, Toraille L, Renaud J, Occelli F, Schmidt M, Salord O, Delobbe A, Debuisschert T, Rondin L, Loubeyre P and Roch J F 2019 *Science* **366** 1359

[30] Yip K Y, Ho K O, Yu K Y, Chen Y, Zhang W, Kasahara S, Mizukami Y, Shibauchi T, Matsuda Y, Goh S K and Yang S 2019 *Science* **366** 1355

[31] Ho K O, Leung M Y, Jiang Y, Ao K P, Zhang W, Yip K Y, Pang Y Y, Wong K C, Goh S K and Yang S 2020 *Phys. Rev. Appl.* **13** 024041

[32] Yu S J, Kang M W, Chang H C, Chen K M and Yu Y C 2005 *J. Am. Chem. Soc.* **127** 17604

[33] Chen J, Deng S Z, Chen J, Yu Z X and Xu N S 1999 *Appl. Phys. Lett.* **74** 3651

[34] Zhang Z, Lin C, Yang X, Tian Y, Gao C, Li K, Zang J, Yang X, Dong L and Shan C 2021 *Carbon* **173** 427

[35] Chen Y C, Salter P S, Knauer S, Weng L, Frangeskou A C, Stephen C J, Ishmael S N, Dolan P R, Johnson S, Green B L, Morley G W, Newton M E, Rarity J G, Booth M J and Smith J M 2017 *Nature Photon.* **11** 77

[36] Maze J R, Stanwix P L, Hodges J S, Hong S, Taylor J M, Cappellaro P, Jiang L, Dutt M V G, Togan E, Zibrov A S, Yacoby A, Walsworth R L and Lukin M D 2008 *Nature* **455** 644

[37] Taylor J M, Cappellaro P, Childress L, Jiang L, Budker D, Hemmer P R, Yacoby A, Walsworth R and Lukin M D 2008 *Nat. Phys.* **4** 810

[38] Bian K, Zheng W, Zeng X, Chen X, Stöhr R, Denisenko A, Yang S, Wrachtrup J and Jiang Y 2021 *Nat. Commun.* **12** 2457

[39] Kucsko G, Maurer P C, Yao N Y, Kubo M, Noh H J, Lo P K, Park H and Lukin M D 2013 *Nature* **500** 54

[40] Doherty M W, Struzhkin V V, Simpson D A, McGuinness L P, Meng Y, Stacey A, Karle T J, Hemley R J, Manson N B, Hollenberg L C L and Prawer S 2014 *Phys. Rev. Lett.* **112** 047601

[41] Hilberer A, Toraille L, Dailledouze C, Adam M P, Hanlon L, Weck G, Schmidt M, Loubeyre P and Roch J F 2023 *Phys. Rev. B* **107** L220102

[42] Ivády V, Simon T, Maze J R, Abrikosov I A and Gali A 2014 *Phys. Rev. B* **90** 235205

[43] Yang X, Dong L, Shan C, Sun J, Zhang N, Wang S, Jiang M, Li B, Xie X and Shen D 2017 *Adv. Mater.* **29** 1602832

[44] Mitra S S, Brafman O, Daniels W B and Crawford R K 1969 *Phys. Rev.* **186** 942

[45] Lv C, Yang X, Wu Y, Lei F, Liang Y, Yang D, Sui L, Qin J, Wu Q, Lai S, Liu H, Zang J, Cheng S, Liu K and Shan C 2025 *Nat. Commun.* **16** 1913

[46] Decremps F, Pellicer-Porres J, Saitta A M, Chervin J C and Polian A 2002 *Phys. Rev. B* **65** 092101